# UV Emission from Lanthanide-Doped Upconversion Nanoparticles in Super-resolution Microscopy: Potential for Cellular Damage

Afshin Karami[1*], Thomas J. de Prinse[2], Nigel A. Spooner[2,3], Stephen P. Kidd[4,5], Christopher J. Sumby[6*]and Jingxiu Bi[1]

[1] *School of Chemical Engineering and Advanced Materials, The University of Adelaide, Adelaide, SA, 5005, Australia*

[2] *Institute for Photonics and Advanced Sensing (IPAS), School of Physical Sciences, The University of Adelaide, Adelaide, 5005, Australia*

[3] *Defence Science and Technology Group, Edinburgh, 5111, Australia*

[4] *Australian Centre for Antimicrobial Resistance Ecology, The University of Adelaide, Adelaide, 5005, Australia*

[5] *Research Centre for Infectious Disease, School of Biological Sciences, The University of Adelaide, Adelaide, 5005, Australia*

[6] *Department of Chemistry and Centre for Advanced Nanomaterials, The University of Adelaide, Adelaide, 5005, Australia*

* Corresponding authors: afshin.karami@adelaide.edu.au, christopher.sumby@adelaide.edu.au

**Keywords:** super-resolution imaging, upconversion nanoparticle probes, stimulated emission depletion (STED) nanoscopy, live cell imaging, ultraviolet (UV) light, cell photodamage

# ABSTRACT

Upconversion nanoparticles (UCNPs) co-doped with lanthanide ions have recently attracted significant attention as fluorescent probes for super-resolution microscopy (SRM). This is due to the advantages of UCNPs over other fluorescence probes, such as fluorescent proteins, owing to their unique optical properties, limited photobleaching and sharp emissions. However, the concurrent emission of ultraviolet (UV) wavelength radiation by UCNPs and the potential for cell photodamage, which may limit useful live cell analysis, have been overlooked. Here, UCNPs synthesised with eight commonly used combinations of Yb/Tm and Yb/Tm/Gd dopants were excited by either pulsed or continuous wave (CW) lasers to evaluate their UV emission. The ratio of emitted UV-A and UV-B were measured relative to blue emission at 475 nm, which is traditionally used for imaging during SRM. We demonstrate that most UCNP samples emit UV light and that the dopant concentration has a key role in generating UV emissions. In addition, the use of pulsed or CW lasers for excitation could lead to a large variation in the amount of UV emitted. This work highlights the importance of considering upconversion dopant composition and concentration, as well as analysing the emission of synthesised UCNPs before their use to prevent unwanted cell photodamage during live cell imaging by SRM. Moreover, it established a need to improve the visible light emission of UCNPs with respect to UV emission for SRM applications.

# INTRODUCTION

Fluorescence microscopy is a widespread tool used to enhance our understanding of biological interactions, especially spatial organization.[1] It visualises the physiological details and interactions of biological molecules with high sensitivity in real-time whilst being a low-invasive technique.[2] However, fluorescence microscopes are characterized by their spatial resolution limitation of 200 nm. This limitation is enforced by the light diffraction limit rationalised by Abbe's rule.[3] This weakness has limited the use of these microscopes as an effective tool in biological sciences for the study of nanosized bio-structures, such as neurons and cytoskeletons. The development of super-resolution microscopy (SRM) techniques has solved the resolution limitations of fluorescence microscopy.[4] The prime technique in SRM is stimulated emission depletion (STED), implemented by either pulsed or continuous wave (CW) lasers.[5-7] The SRM approaches rely upon fluorescence probes that are capable of emission upon excitation by light in an intensity range from $W/cm^2$ to $GW/cm^2$ (compared with fluorescence microscopy at $mW/cm^2$ to $W/cm^2$) and a specific wavelength, while being photostable.[8]

Recently, lanthanide ion-doped upconversion nanoparticle (UCNP) probes have gained attention for SRM over the traditionally used organic fluorophores.[9] The UCNP probes have advantages including sharp and tuneable light emission, long lifetimes, low background autofluorescence and limited photobleaching.[10] The most common co-doped UCNP ion pairs used as a probe in SRM are $Yb^{3+}$ and $Tm^{3+}$.[11] Yb/Tm based UCNPs produce bright emissions in the blue region at 475 nm when excited by near-infrared (NIR) light at 980 nm. The NIR photon is absorbed by the $Yb^{3+}$ ion (sensitizer) and transferred sequentially to the $Tm^{3+}$ ion (activator), with consecutive energy transfer events exciting the $Tm^{3+}$ ion into the emissive $^1D_2$ state. The $^1D_2$ state then emits blue fluorescence at 450 nm, undergoing a $^1D_2 \rightarrow {}^3F_4$ transition.

Additionally, this excitation pathway promotes a $^1G_4 \rightarrow {}^3H_6$ transition that emits fluorescence at 475 nm. The blue emissions at 450 and 475 nm are imaged together through a NIR short pass blocking filter in a microscopy setting due to the similar wavelength of these emissions. Continual development of Yb/Tm doped UCNPs to achieve brighter blue emissions suitable for imaging in SRM has been pursued.[12] In that work, the focus has been on improving the efficiencies of photon transfer processes and the lifetimes of the sequential $Tm^{3+}$ excited states.[13,14] A high concentration of $Yb^{3+}$ sensitizer improves the transfer of the photon to $Tm^{3+}$ in Yb/Tm doped UCNPs, while the core/shell structure of Yb/Tm UCNPs reduces surface quenching effects, hence improving the upconversion efficiency.[15,16] These strategies have been implemented to produce brighter blue light emission from a given power density of 980 nm excitation light.[17] However, this improvement in the blue fluorescence yield has a drawback. The energy transfer process continues past the blue, generating fluorescence in the ultraviolet (UV) range (wavelengths 280 to 400 nm). Thus, Yb/Tm doped UCNPs imaged near or inside of cells will have the ability to emit UV light in this wavelength range too.

While some studies intentionally generate UV light from UCNPs to directly influence or kill cells[18-20], most imaging applications do not consider the emissions in this range. This raises questions as to whether some UCNPs have significant energetic UV emissions that are not being detected, commonly due to most spectral systems having difficulty readily characterising UV emissions. While UV emissions are rarely studied and do not contribute to standard imaging experiments, UV emission is potentially damaging to the cells under study at such close range.

The UV light spectral region is subdivided into three distinct regions UV-A (wavelengths between 320 to 400 nm), UV-B (wavelengths between 280 to 320 nm) and UV-C (wavelengths between 200 to 280 nm).[21] UV light causes cell phototoxicity by intracellular interactions or

generating reactive oxygen species (ROS) that consequently cause oxidative damage to the cell. DNA strand break and thymidine dimerisations, UV response activation apoptosis and toxic reactive oxygen species (ROS) generation (endogenous and exogenous) have been identified as the main causes of cell damage by UV light (Scheme 1).[22]

Scheme 1. Excitation of lanthanide-doped upconversion nanoparticles (UCNPs) with near-infrared (NIR) light and the associated upconversion emissions in the UV-A, B and visible regions. The $Yb^{3+}$ is shown as blue and $Tm^{3+}$ in pink in the UCNP in the scheme. The visible emissions at 450 and 475 nm are desired for super-resolution microscopy (SRM); however, certain lanthanide-doped materials, such as Tm/Yb doped UCNPs, also emit UV-A and UV-B light. The potential cell damage by the emitted UV light is presented when it causes damage to biological molecules, e.g. DNA strand breakage/base dimerization, initiates apoptotic pathways, or interacts with endogenous (e.g. NADH) or exogenous (e.g. GFP) molecules to generate reactive oxygen species. Components adapted with permission from Ref.[22]. Copyright 2020 IOP Publishing Ltd. Created with BioRender.com.

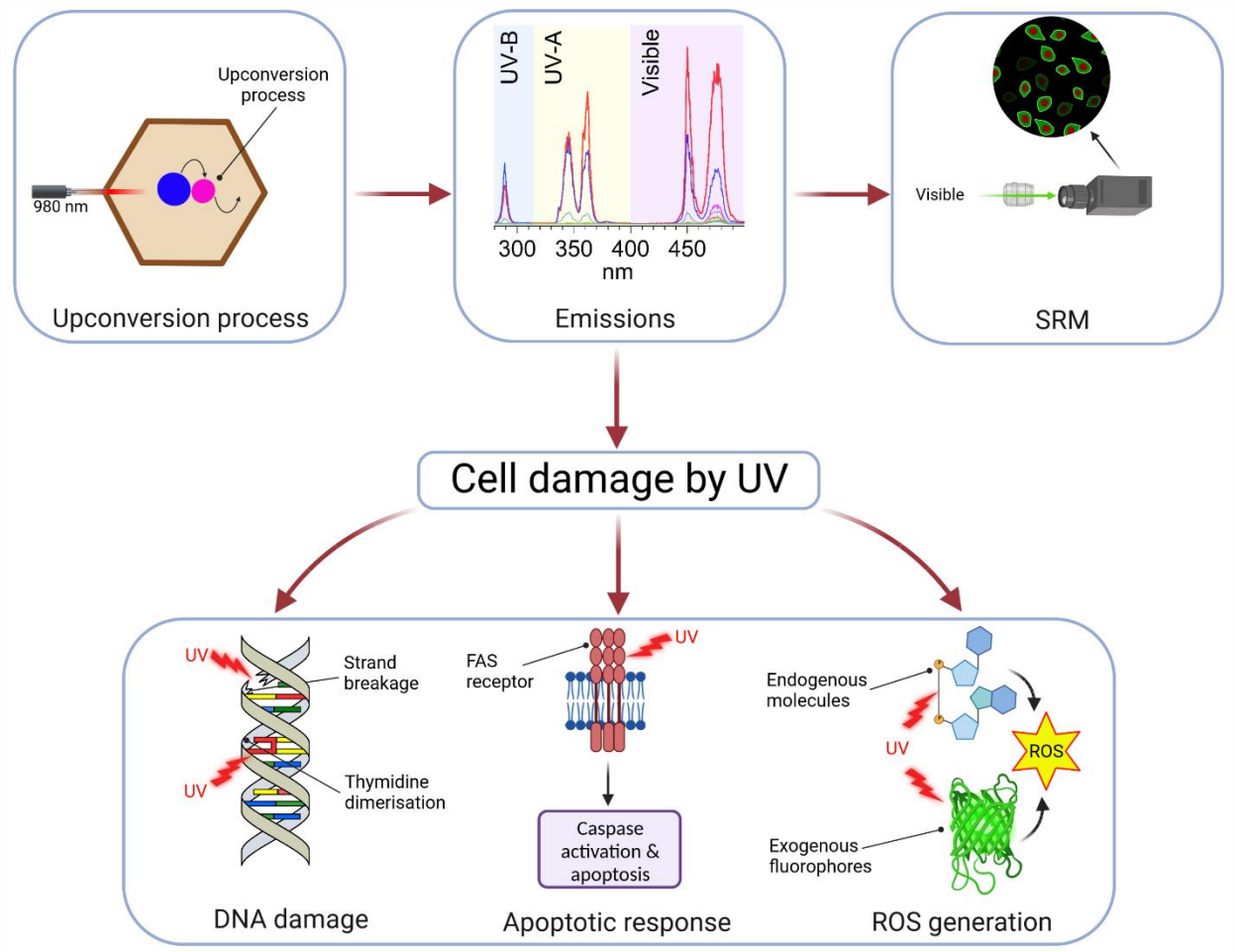

This paper reports the UV emission properties for several UCNPs designed for SRM applications. Eight UCNPs, based on $NaYF_4$:Yb/Tm, $NaYbF_4$:Tm and $NaYbF_4$:Tm/Gd structures, were synthesized and characterized for this purpose. The presence and extent of UV emissions under continuous and pulsed excitation regimes were measured using UV sensitive detector systems, with the potential negative impact of high energy emissions from these UCNPs on a surrounding biological sample discussed. The findings from this work suggest that a correct measurement of emission across the UV range, in addition to the targeted visible emission measurements, should be strongly considered when developing UCNPs for SRM applications.

## RESULTS AND DISCUSSION

**Synthesis, composition, and morphology.** Lanthanide-doped UCNPs, NaYb(100-x%)$F_4$:Tm(x%) (x = 1, 2.5, 5 and 10 mol%), NaY(100-x%)$F_4$:Yb(18%)/Tm(x%) (x = 1 and 5 mol%) and NaYb(100-x%)$F_4$:Tm(0.5%)/Gd(x%) (x = 5 and 20 mol%), were synthesized via the thermolysis method (Scheme 2).[23]

Scheme 2. Methods used to synthesize the lanthanide-doped upconversion nanoparticles. (a) Synthetic procedure for hexagonal β-$NaYF_4$:Yb/Tm materials and (b) for hexagonal β-$NaYbF_4$:Tm UCNPs. Created with BioRender.com.

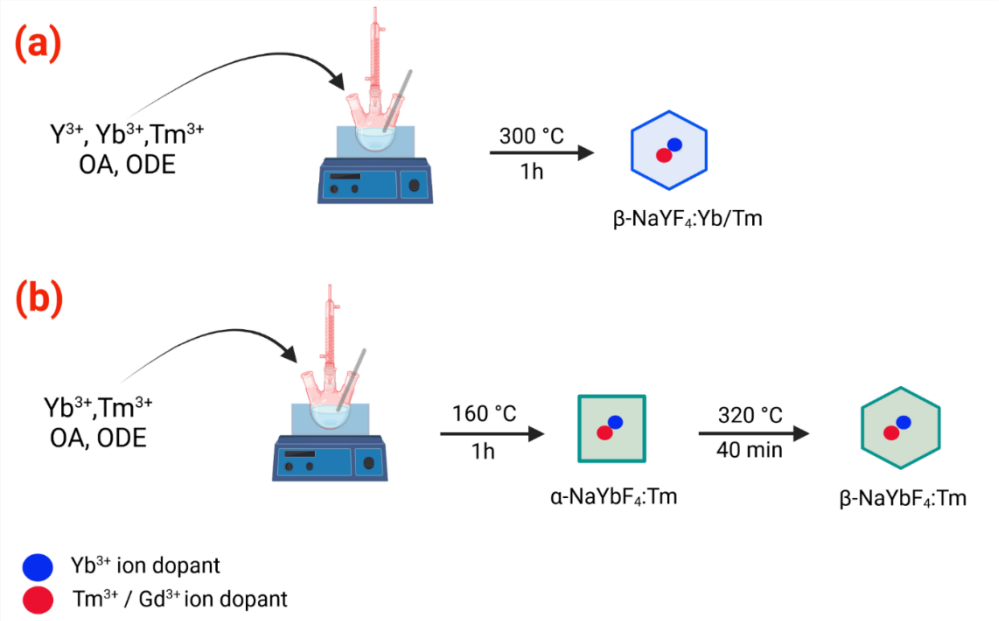


Powder X-ray diffraction (PXRD) data for NaYb(100-x)$F_4$:Tm(x) and NaY(100-x%)$F_4$:Yb(18%)/Tm(x%) samples confirmed all materials are crystalline, with the diffraction peaks indexed to the hexagonal β-$NaYbF_4$ (# 27-1427) and hexagonal β-$NaYF_4$ (# 16-0334) structures (Figure 1a and Table S1). The only exception is nanoparticle sample NaYb(90%)$F_4$:Tm(10%) which shows a small trace of the cubic structure of α-$NaYbF_4$ (# 77-2043) (Figure 1a and Table S1). The 5% Gd loaded sample of NaYb(100-x)$F_4$:Tm(0.5%)/Gd(x) shows diffraction peaks that match a mixture of hexagonal β-$NaYbF_4$ (# 27-1427) and cubic α-$NaYbF_4$ (# 77-2043) structures (Figure 1a and Table S1). In comparison, the sample with 20% Gd loading shows a predominately hexagonal structure with a small trace of the cubic structure (Figure 1a and Table S1). In the presence of $Gd^{3+}$, the formation of a phase pure hexagonal β-$NaYbF_4$ host material by the thermolysis method was challenging despite using a well-

established two-step synthesis procedure (160°C for 1 hour to form the cubic α-phase, then 320°C for 40 minutes to convert cubic α-phase to hexagonal β-phase). Potentially, this issue could be overcome by adjusting the synthesis protocol, including the ratio of OA to ODE, the synthesis time, the use of different precursor salts, etc. As altering the synthesis parameters may affect the surface chemistry of the NP samples, leading to different emissions, we avoided this approach.

Transmission electron microscopy (TEM) images revealed that the synthesized UCNPs are uniformly sized, as shown by the mean particle sizes for each NP sample (Figure 1b to i, Table S1 and Figure S9-11). The as-synthesised hexagonal $NaYbF_4$ based samples are larger, as expected, as increasing the $Yb^{3+}$ concentration and the synthesis time will normally lead to an increase in particle size (Figure 1d to g, S9-11). While this could be overcome by increasing the oleic acid (OA) to 1-octadecene (ODE) ratio in the synthesis and altering the other synthesis parameters,[24] the same ratio of OA to ODE was used in the synthesis of all NPs for consistency. The composition of the nanoparticles, primarily determined by the feed ratios of the components, was confirmed by Energy Dispersive Spectroscopy (EDS) as well as inductively-coupled plasma mass spectrometry (ICP-MS). EDS analysis showed that the Tm concentrations were approximately 1 and 5 mol%, as expected, in the $NaY(100\text{-}x\%)F_4$:Yb(18%)/Tm(x%) (x= 1 and 5 mol%) NP samples, respectively (Table S1 & Figure S1 to S2). The Tm dopant concentration was measured to be 1, 2, 5 and 11% for the $NaYb(100\text{-}x\%)F_4$:Tm(x%) (x=1, 2.5, 5 and 10 mol%) NP samples, respectively (Table S1 & Figure S3 to S6). Finally, the Gd concentration was also measured to be 5 and 28%, while the Tm concentrations were found to be negligible for $NaYb(100\text{-}x\%)F_4$:Tm(0.5%)/Gd(x) (x=5 and 20 mol%) NP samples, respectively (Table S1 & Figure S7 to S8. Note that the figures in Figures S1 to S8 show SEM-EDS measurement results

rounded to whole numbers). In the SEM-EDS, Tm and Gd elemental doses were calculated based on Yb values and Tm/Yb and Gd/Yb ratios. ICP-MS data for the UCNP samples supported these results, confirming Tm concentrations of 0.9% and 4.8% in NaY(100-x%)$F_4$:Yb(18%)/Tm(x%) (x= 1 and 5 mol%), respectively (Table S1 & S2). Similarly, the Tm dopant concentration was measured to be 1.0, 2.5, 5.0 and 10.1% for the NaYb(100-x%)$F_4$:Tm(x%) (x=1, 2.5, 5 and 10 mol%), respectively. Finally, the Gd concentrations were found 4.9 and 20.0% while the Tm concentrations were 0.4 and 0.3% for NaYb(100-x%)$F_4$:Tm(0.5%)/Gd(x) (x=5 and 20 mol%) NP samples, respectively. Overall, the combined EDS and ICP-MS results confirmed that the Tm and Gd dopant concentrations broadly matched those used in the synthesis, and moreover, that the distribution of dopants was relatively homogenous, e.g. surface-sensitive EDS data matched that for the bulk sample determined by ICP-MS.

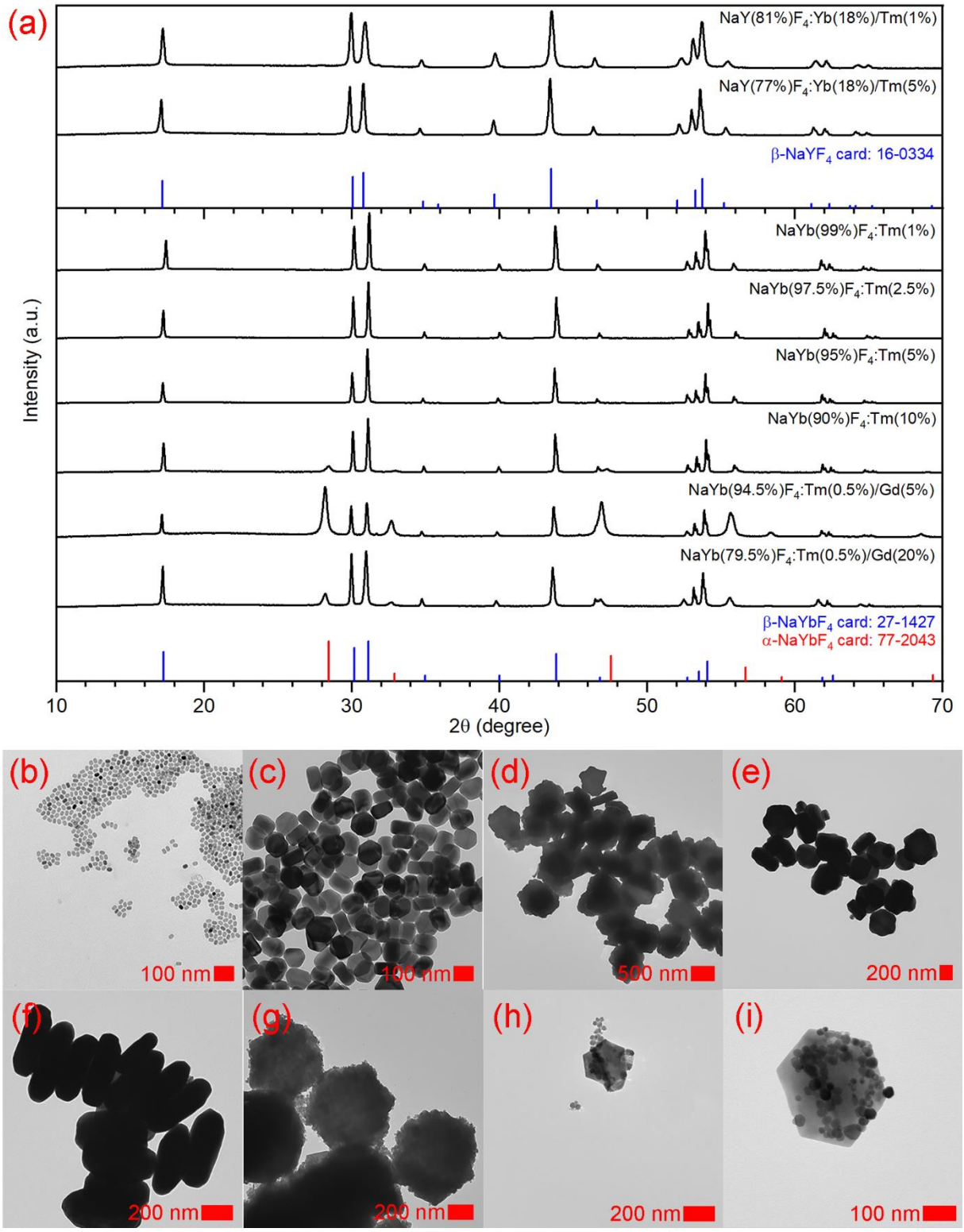


Figure 1. PXRD data and TEM images for the as-synthesised UCNP samples. (a) PXRD data for the NaYb(100-x)$F_4$:Tm(x) (x=1, 2.5, 5 and 10 mol%), NaY(100-x%)$F_4$:Yb(18%)/Tm(x%)(x=1

and 5 mol%) and NaYb(100-x)$F_4$:Tm(0.5%)/Gd(x) (x= 5, 16.5, and 20 mol%) UCNP samples. The PDF cards for α-$NaYF_4$ # 06-0342, β-$NaYF_4$ # 16-0334, α-$NaYbF_4$ # 77-2043 and β-$NaYbF_4$ # 27-1427 are also presented. (b) TEM images for the as-synthesised hexagonal structure of β-NaY(81%)$F_4$:Yb(18%)/Tm(1%), (c) hexagonal structure of β-NaY(77%)$F_4$:Yb(18%)/Tm(5%), (d) hexagonal structure of β-NaYb(99%)$F_4$:Tm(1%), (e) hexagonal structure of β-NaYb(97.5%)$F_4$:Tm(2.5%), (f) hexagonal structure of β-NaYb(95%)$F_4$:Tm(5%), (g) hexagonal structure of β-NaYb(90%)$F_4$:Tm(10%). The β-NaYb(90%)$F_4$:Tm(10%) UCNP sample shows a small trace of the cubic structure of α-$NaYbF_4$ while the majority of the sample is hexagonal structure β-NaYbF4 as confirmed by the PXRD data, (h) NaYb(94.5%)$F_4$:Tm(0.5%)/Gd(5%). The NaYb(94.5%)$F_4$:Tm(0.5%)/Gd(5%) UCNP sample shows a mixture of hexagonal β-$NaYbF_4$ and cubic α-$NaYbF_4$ structures, (i) NaYb(79.5%)$F_4$:Tm(0.5%)/Gd(20%) UCNP. The NaYb(79.5%)$F_4$:Tm(0.5%)/Gd(20%) UCNP sample shows a small trace of the cubic structure α-$NaYbF_4$ while the majority of the sample is hexagonal β-$NaYbF_4$ as confirmed by the PXRD data.

**Excitation Power Density Used.** UCNP samples can be excited by continuous laser sources, which offer high average power, or by pulsed lasers, which offer relatively low average power but can produce a large amount of light in a short period. Both pulsed and CW lasers are routinely used to excite UCNPs in microscopy; however, the behaviour of an upconversion material often changes depending on the power regime used (high average power or high peak power). To investigate this, different excitation lasers were used to excite the samples studied, with a CW diode laser allowing high average power and a pulsed optical parametric oscillator producing high peak excitation power. The CW measurements were conducted using a 980 nm solid-state diode laser with its power adjustable over 50 mW to 2 W. The emission spectra of the

samples were collected at 75 mW spread over a beam spot size of 40 $mm^2$, exciting the samples at a power density of 0.185 $W/cm^2$. This laser was additionally used in the CW slope dependence measurements up to a maximum value of 4.5 $W/cm^2$. In comparison, the spectra for the samples under high peak power excitation were produced by a flashlamp pumped optical parametric oscillator (OPO) laser set at 980 nm which fired pulses 5 ns in length at 20 Hz. The laser had an energy of 0.8 mJ per pulse and was focused down to a spot size of 2 mm, resulting in a peak power of 0.16 MW and a power density of 5.1 $MW/cm^2$. A second OPO laser was used for the high peak power slope dependence measurements due to its wider accessible range pulse of energies. This OPO fired pulses of 5 ns in length at 10 Hz with maximum energy at 980 nm of 7.5 mJ over a 5 mm diameter beam, giving a peak power density approaching 8 $MW/cm^2$.

While optical techniques can vary greatly between research groups, the excitation power densities used in this paper (hundreds of $mW/cm^2$ to several $W/cm^2$ for CW excitation and several $MW/cm^2$ for pulsed excitation) is representative of many examples of UCNP excitation and STED microscopy.[25-27]

**Emission spectra.** To examine the factors that govern the presence and extent of UV emission for UCNPs, including nanoparticle composition and excitation mode, the synthesised UCNPs were excited under continuous and pulsed excitation regimes and the emission was measured using a visible and UV sensitive detector system. The power density for the pulsed and CW lasers was kept unchanged for the excitation of all NP samples to allow comparison of the emissions. The NaYb(99%)$F_4$:Tm(1 mol%) and NaYb(97.5%)$F_4$:Tm(2.5 mol%) NP samples were the brightest of the eight samples with strong blue emissions at 450 and 475 nm. These also gave UV-A and B emissions at 289, 345 and 361 nm when excited by the pulsed laser (Figures 2a, b and c). Under non-saturated conditions, UV emission is considerably less likely than blue

emission, due to the UV emission requiring additional transfers of energy from the sensitizer ion ($^1G_4 \rightarrow {}^3H_6 \propto I_{ex}{}^3$ (475 nm), $^1D_2 \rightarrow {}^3F_4$, $^1D_2 \rightarrow {}^3H_6 \propto I_{ex}{}^4$ (455, 362 nm), $^1I_6 \rightarrow {}^3F_4$, $^1I_6 \rightarrow {}^3H_6 \propto I_{ex}{}^5$ (345, 289 nm)). If this model for excitation is used, any UV lines shorter than 362 nm would have low intensities relative to the blue emission lines. However, due to the high sensitizer ($Yb^{3+}$) to activator ($Tm^{3+}$) ion ratio, a saturation of the Tm energy levels results in much higher UV emission than a non-saturated model suggests. The $^1I_6 \rightarrow {}^3H_6$ peak has a significantly lower intensity than the other transitions and, as such, this emission line is difficult to observe for any other samples. Similar to the data with the pulsed laser, in a CW laser excitation experiment, the NaYb(99%)$F_4$:Tm(1%) and NaYb(97.5%)$F_4$:Tm(2.5 mol%) again showed among the strongest blue wavelength emissions (Figure 2d and e), although NaY(81%)$F_4$:Yb(18%)/Tm(1%) and NaYb(94.5%)$F_4$:Tm(0.5%):Gd(5%) samples had relatively brighter blue emission. CW excitation of the Gd doped samples showed a noticeable emission peak at 311 nm, compared with pulsed laser excitation, with a much lower excitation intensity.

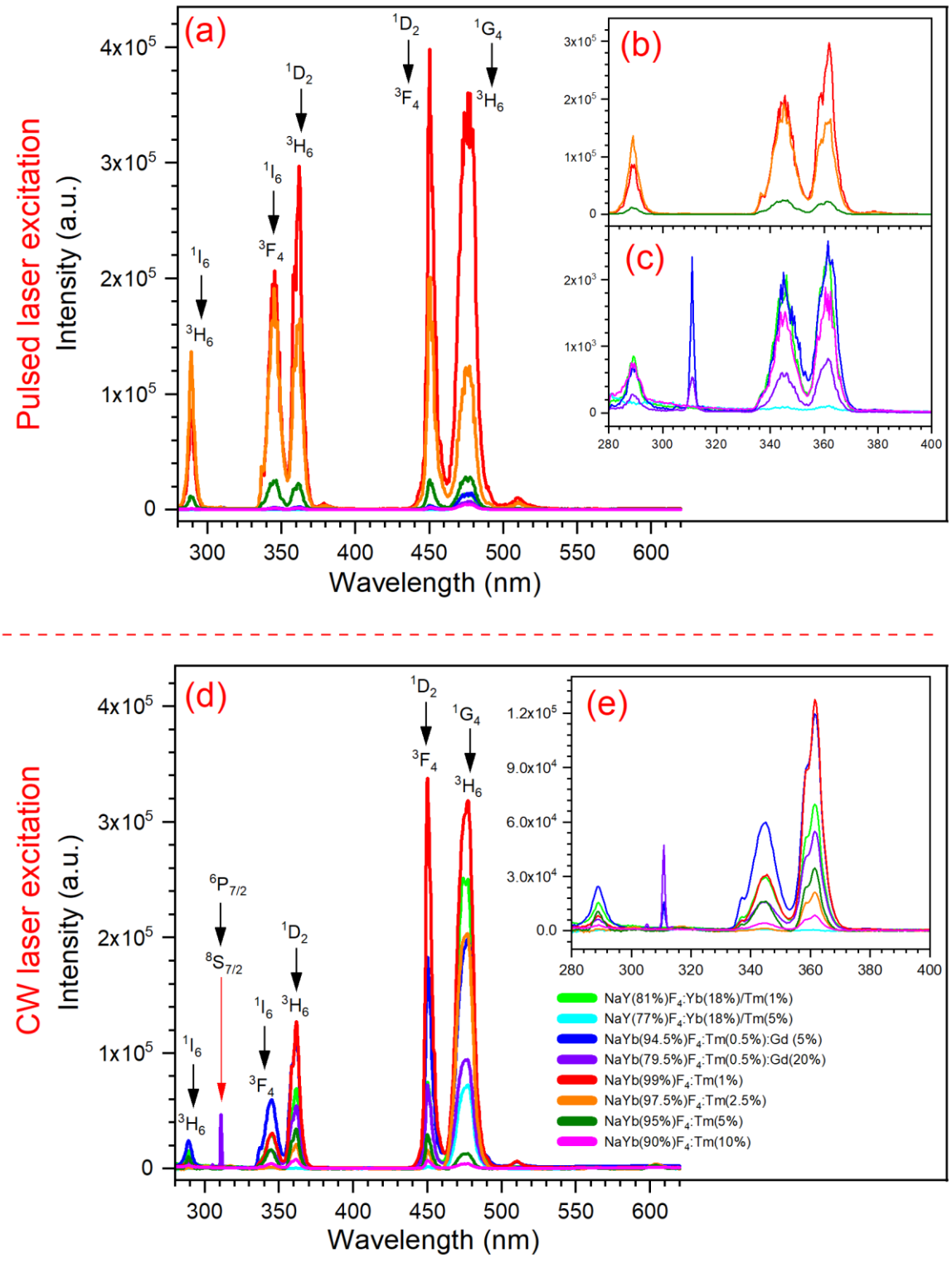


Figure 2. Emission spectra for UCNP samples excited by pulsed and CW lasers. (a) Emission spectra for pulsed laser excitation, and (b and c) enlargements of the emission spectra for the

UV-A and B regions for brightest and less bright NP samples excited by pulsed laser. (d) Emission spectra for CW laser excitation, and (e) enlargement of the emission spectra for the UV-A and B emissions excited by CW laser.

The emission peaks from UCNP samples were further analysed to assess the significance of the UV emission relative to the blue emission. For this purpose, first, the peak intensity for each sample was extracted and presented based on dopant concentration changes (Figures 3a and c, 4a and c, 5a and c). Then the ratio of combined peaks in the UV-A (320 to 400 nm) and UV-B (280-320 nm) ranges to the blue (475 nm) peak for each sample was calculated, based on the area under the curve for each peak (Figure 3b and d, 4b and d, 5b and d). For the NaY(100-x%)$F_4$:Yb(18%)/Tm(x%) (x = 1 and 5 mol%) samples, the 1% Tm doped sample showed higher peak intensity for the 289, 345 and 361 nm peaks, when excited by pulsed laser (Figure 3a). The UV-A ratio to 475 nm peak was also much higher than the UV-B ratio for the 1% Tm sample in the pulsed laser excitation mode (Figure 3b). This result reveals that in $NaYF_4$ UCNPs, a lower Tm composition may lead to a higher chance of generating UV emissions. This behaviour could be due to a reduced number of emitting ions and this appears to be suppressed by increasing the Tm doping. A similar observation occurs when the NP samples were excited by the CW laser (Figures 3c and d). The emission peak intensity for the 1% Tm sample again showed a higher value than the 5% Tm sample (Figure 3c). The 1% Tm sample showed a larger UV-A to 475 nm emission ratio (Figure 3d), while the ratio of UV-B to 475 nm is similar for both 1 and 5% Tm samples under CW laser excitation (Figure 3d), highlighting the importance of irradiation setup.

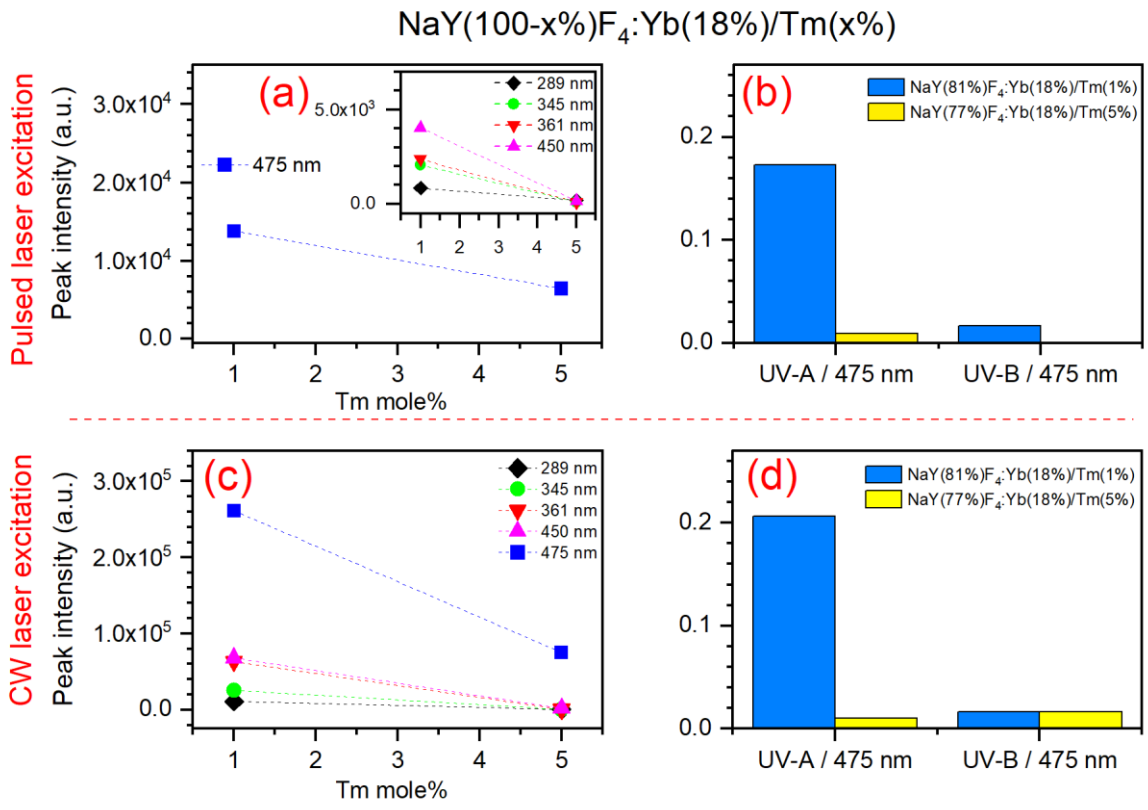


Figure 3. Emission peak intensities and ratios of UV-A and B to the 475 nm peak for NaY(100-x%)$F_4$:Yb(18%)/Tm(x%) (x = 1 and 5 mol%). (a) Emission peak intensity data excited by the pulsed laser, with the lower emission peaks are shown in the inset, (b) ratios of UV-A and B to the 475 nm peak excited by the pulsed laser, (c) emission peak intensity data excited by the CW laser, and (d) ratios of UV-A and B to the 475 nm peak excited by the CW laser.

For samples of composition NaYb(100-x%)$F_4$:Tm(x%) (x = 1, 2.5, 5 and 10 mole%) excited by the pulsed laser, the intensity of emission at 345, 361, 450 and 475 nm declines upon increasing the Tm loading from 1% to 10% (Figure 4a). This reduction in brightness can be explained by the combined effects from quenching caused by higher activator concentration ($Tm^{3+}$) and improved upconversion efficiency by increasing the sensitizer concentration ($Yb^{3+}$).[28,29] Interestingly, despite the 1% Tm loaded sample giving the most intense emission

overall, the sample with 2.5% Tm loading showed the highest ratio of UV-A and B to 475 nm emission among all four samples excited by pulsed laser (Figure 4b). This is due to the 475 nm peak in the 1% Tm loaded sample having a considerably higher emission intensity compared with the other samples. The ratio of UV-A and B to 475 nm emission decreased in the following order: 2.5 > 5 > 1 > 10% Tm doped samples, respectively (Figure 4b). This result demonstrates that although the sample with 1% Tm loading gives the most intense emission among these four samples (Figures 2a and 4a), the 2.5 and 5% Tm doped NP samples emit a larger proportion of UV radiation.

For excitation with the CW laser, again the sample with 1% Tm loading showed the most intense emissions at 345, 361, 450 and 475 nm among all these NP samples (Figure 4c), while the NP samples with 5 and 10% Tm loading showed the highest ratio of UV-A and B to 475 nm emission, respectively (Figure 4d). These results reveal that both the ratio of emissions at particular wavelengths and the emission intensities need to be considered to reduce the probability of phototoxicity in SRM applications. Of the four $NaYb(100\text{-}x\%)F_4:Tm(x\%)$ NP samples excited by the pulsed laser, both lower (1%) and higher (10%) doping leads to less pronounced UV emission relative to the desired 475 nm emission. However, the 475 nm emission is notably brighter for the 1% Tm sample (Figures 4a). In contrast, when these four samples are excited by the CW laser, the sample with 2.5% doping emits less UV emission relative to the 475 nm emission, while the 5% Tm doped sample emits the most intense UV emission relative to the 475 nm emission, definitively highlighting the importance of considering how the UCNPs are excited in an SRM application (Figure 4c and d).

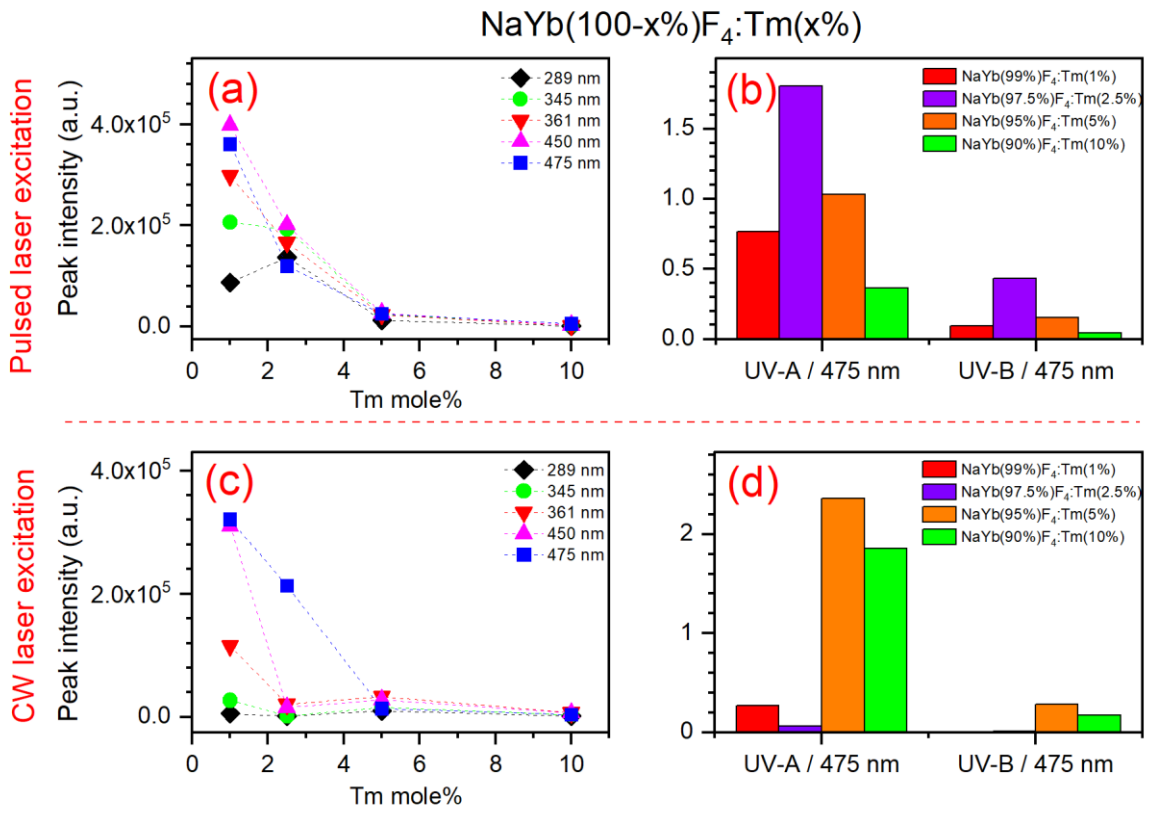


Figure 4. Emission peak intensities and ratios of UV-A and B to the 475 nm peak for NaYb(100-x%)$F_4$:Tm(x%) (x = 1, 2.5, 5 and 10 mol%). (a) Emission peak intensity data excited by the pulsed laser, (b) ratios of UV-A and B to the 475 nm peak excited by the pulsed laser, (c) emission peak intensity data excited by the CW laser, and (d) ratios of UV-A and B to the 475 nm peak excited by the CW laser.

Gd-doped UCNPs have attracted attention recently as a fluorescent probe for STED microscopy due to their ability to reduce depletion saturation intensity. Gd dopants create massive energy migration networks that move energy from the luminescent centre to surface quenchers. Consequently, STED microscopy using these nanoparticles benefits from a lower-intensity light source to deplete photons.[30] While, the Gd dopant in UCNP has addressed a fundamental problem with STED microscopy (high-intensity depletion), it also produces UV

emission at 311 nm. With Yb/Tm co-doped UCNP exhibiting UV emission, we used $NaYbF_4$ host structure to investigate Gd effects on UV generation. In these UCNP samples, the $Tm^{3+}$ concentration was reduced from 1 mmole to 0.5 mmole to emphasize $Gd^{3+}$ effects.

As the PXRD results (Figure 1a) demonstrated for the as-synthesized Gd-doped UCNP samples, a quantity of the α-$NaYbF_4$ host possesing a cubic crystal structure was formed in addition to the desired hexagonal β-$NaYbF_4$ crystal host phase. In the emission investigation conducted herein, the cubic α-$NaYbF_4$ crystal form is considered to be essentially silent and should not contribute to the emissions. Due to their structures, hexagonal β-$NaREF_4$ crystal structures (RE= rare earth, e.g. β-$NaYbF_4$ and β-$NaYF_4$) are generally regarded as more efficient than their cubic counterparts.[31-33] In both of these host UCNPs, emission from the cubic phase is extremely weak, due to a number of structural differences. In particular, the hexagonal β-$NaYF_4$ crystal structure has lanthanide sites in low-symmetry positions where distorted electron clouds are heavily coupled to the lattice. In comparison, the cubic crystal structue has random substitutions between the lanthanide cations and the $Na^+$ ions within the crystal lattice. This inevitably complicates their bonding, and thus the cubic phase suffers from a greater energy loss than the hexagonal phase.[34] Additionally, there is a smaller distance between adjacent lanthanide ions in the hexagonal structure, 3.548 Å compared to 3.868 Å in the cubic form.[31] For these reasons, typically the upconversion efficiency of lanthanide-doped $NaYF_4$ with a cubic structure is considerably lower than that of the hexagonal $NaYF_4$ forms.[34] For example, the hexagonal β-$NaYF_4$ crystal structure facilitates the emission of $Er^{3+}$ lanthanide ions with a four times higher efficiency than cubic α-$NaYF_4$ crystal structure.[33] Although, potentially a Gd-doped UCNP with pure hexagonal $NaYbF_4$ host crystal could be synthesized by adjusting the synthesis procedure, for consistency and to prevent changing the surface chemistry of the as-synthesized UCNPs, the

same synthesis protocol was used to synthesize these NPs resulting in the analysis necessarily involving a small amount of the weakly emitting cubic phase.

For the NaY(100-x%)$F_4$:Yb(18%)/Tm(0.5%)/Gd(x%) (x = 5 and 20 mole%) samples excited by pulsed laser, the emission peaks at 289, 311, 345, 450 and 475 nm for the 5% Gd sample were of higher intensity compared with higher 20% Gd loaded sample (Figure 5a). The new peak observed at 311 nm is due to Gd emission in both samples. Interestingly, the peak intensities for these two samples were notably higher when excited by CW laser (Figure 5c). This in turn leads to a much higher ratio of UV-A and B to 475 nm emission in CW laser excitation mode compared with pulsed laser excitation mode (Figure 5b, d). The UV-A to 475 nm ratio of emission is higher for 5% Gd doped UCNPs, while the UV-B to 475 nm is higher at 20% Gd doped materials in both pulsed and CW laser mode (Figure 5b, d). These results indicate that Gd doping could play a key role in the UV light generation of these NP samples, possibly by the formation of crystal defects. It has been shown previously that crystal defects change the symmetry around the lanthanide emitter ions in the crystal structure, leading to better energy transfer and enhanced upconversion luminescence.[35] Hence, the phototoxicity of the NaYb(100-x%)$F_4$:Tm(0.5%)/Gd(x%) NP samples for SRM applications may directly be correlated with the Gd loading and concomitant changes in the crystal structure.

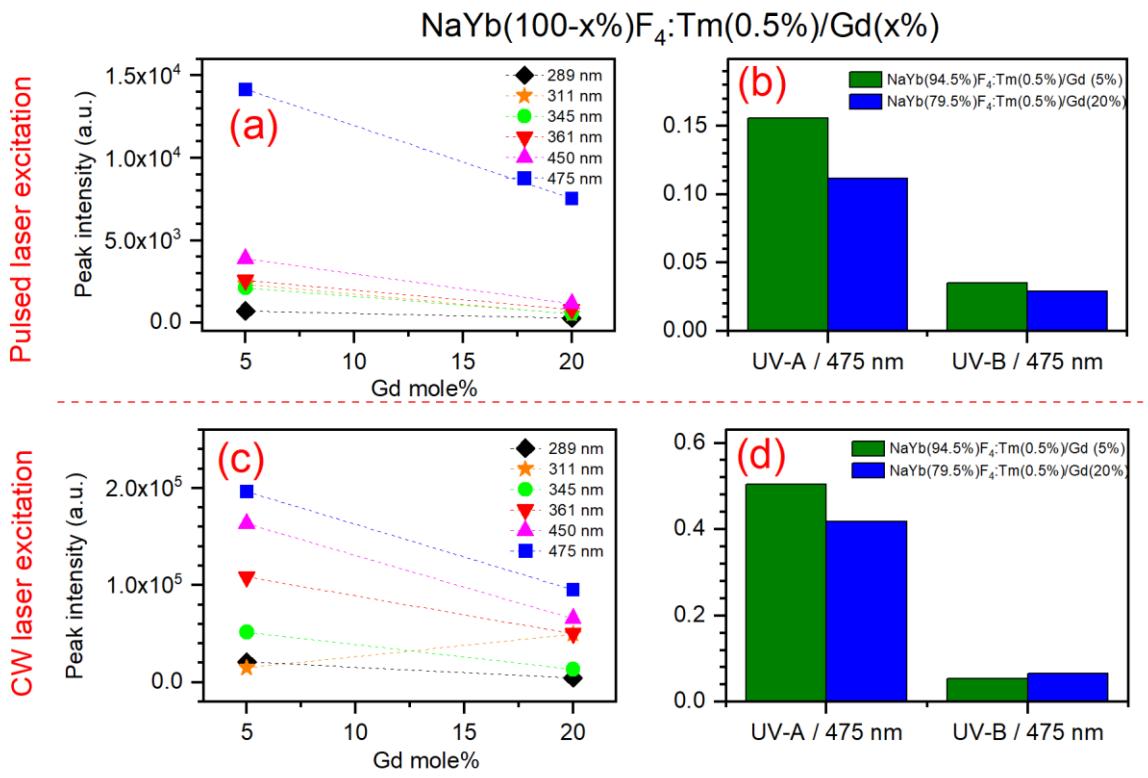


Figure 5. Emission peak intensities and ratios of UV-A and B to the 475 nm peak for NaYb(100-x%) $F_4$: Tm (0.5%)/Gd (x%) (x = 5 and 20 mol%). (a) Emission peak intensity data excited by the pulsed laser, (b) ratios of UV-A and B to the 475 nm peak excited by the pulsed laser, (c) emission peak intensity data excited by the CW laser, and (d) ratios of UV-A and B to the 475 nm peak excited by the CW laser.

The as-synthesised UCNP samples were all confirmed to generate UV emissions in the UV-A and B regions. The UV light generated from the same host crystal structure is directly correlated with the dopant concentration and whether a pulsed or CW laser is used for excitation. The amount of dopant concentration also affects the intensity of blue light emission, which is required for SRM. Therefore, adjusting the dopant concentration and conducting analysis of the emissions of any new UCNPs should provide a route to enhance the blue light emission, whilst

reducing the UV emission, and thereby facilitate the development of more efficient and biologically benign fluorescence probes for SRM.

**Excitation power dependency of visible and UV emission.** In the UCNPs, visible and UV emission is generated from the $Tm^{3+}$ ion by sequential energy transfer from the $Yb^{3+}$ ion. This process involves four energy transfer steps to cause emission from the $^1D_2$ level in $Tm^{3+}$, and five steps to reach the $^1I_6$ level (Figure 6a). This process can be experimentally verified by adjusting the excitation intensity incident on the sample and measuring the change in intensity at each emission wavelength peak.[36] The change in emission compared to excitation intensity is directly proportional to the number of photons being used in the upconversion process,[37] and therefore, when the data is presented in a log-log plot, the power dependency is given by the slope of the excitation/emission curve. The excitation power dependency was measured for all the as-synthesised NP samples. The power dependency for the $NaYb(95\%)F_4:Tm(5\%)$ sample excited by pulsed laser is given in Figure 6b, while the slope values for all samples excited by both pulsed and CW lasers are presented in Tables S3 and S4, respectively. It should be noted that the experimentally determined slope values are less than the ideal values, as is often observed.[38,39] This is primarily due to $Tm^{3+}$ - $Tm^{3+}$ cross relaxation improving the photon efficiency of the system[40] (Figure 6a), especially in the CW case, as well as minor saturation effects at the high intensities used during both CW and pulsed excitation.

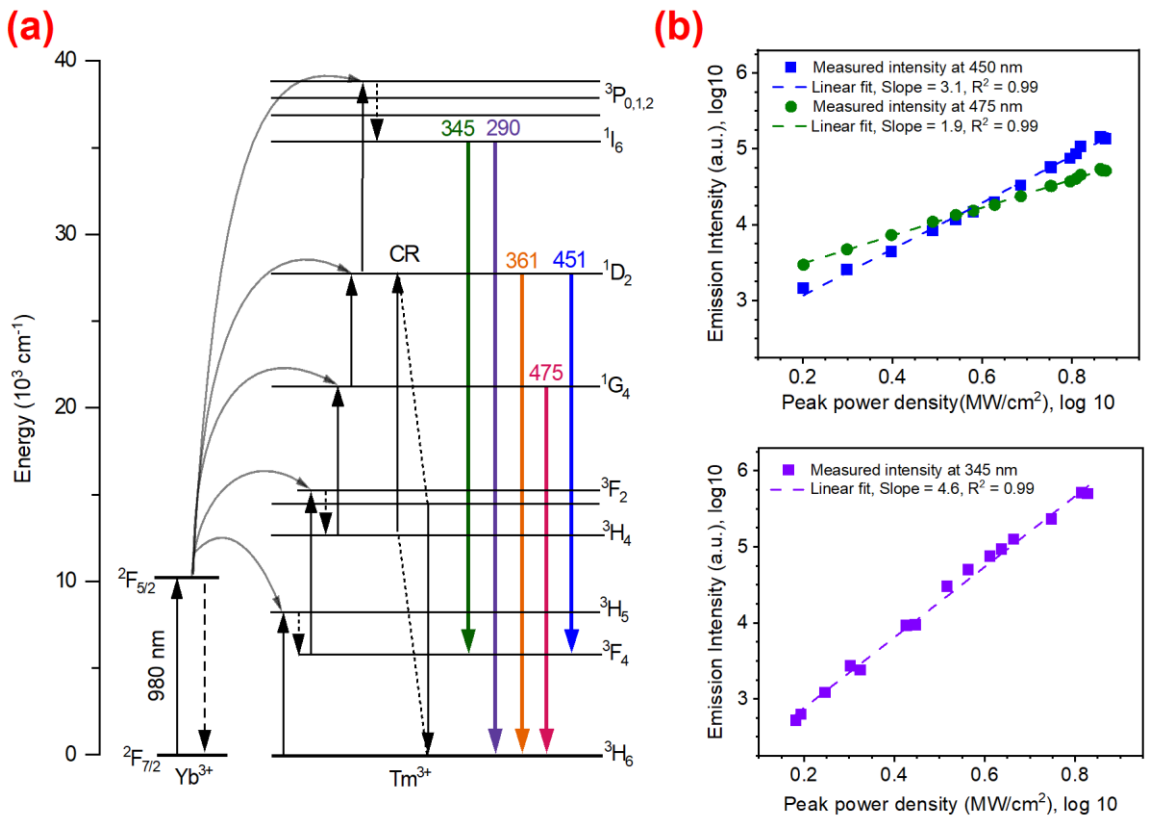


Figure 6. An energy diagram showing an ideal energy transfer process, and power dependence graphs for the UV and blue emissions from NaYb(95%)$F_4$:Tm(5%) excited by the pulsed laser. (a) The schematic shows energy transfer mechanism of $Yb^{3+}$ to $Tm^{3+}$. (b) The observed slope values are less than the ideal values, but the UV energy dependence is clearly higher than either of the visible emissions and no saturation is observed.

These slope values are important as they show that the UV emissions are not uniquely saturated in comparison to the visible emission and that raising the excitation intensity incident on the samples will increase the UV emission more, relative to the visible emission. Considering the NaYb(95%)$F_4$:Tm(5%) case depicted in Figure 6b, if a microscopy experiment required the blue emission at 475 nm to be arbitrarily four times as bright, the excitation laser energy only needs to be increased two times the original intensity due to the 2-photon process occurring. This

two-times increase in excitation power causes the other blue emission to amplify to approximately 8.5 times its original value, however, and the UV peak at 345 nm magnifies to over 25 times as intense. Some reports of STED have utilised CW excitation power densities in excess of what is demonstrated in this report, reaching above the kW/cm$^2$ level.[12,41] Despite the upconversion pathways eventually saturating under these conditions, the UV light generation under this excitation power regime would be even higher than has been demonstrated in this work.

**Difficulties in Correct UV Emission Detection.** It is of high importance for SRM applications of new fluorophores, like UCNPs, that measurement of the UV range be undertaken, as the difficulty of detecting this range can often lead to the erroneous assumption that a lack of detected UV emissions represents a true lack of emissions, with the true emission peaks simply being unobserved. Fluorescence emission can be difficult to detect and quantify in the UV range as a result of the intense absorption of UV light by many materials, including optical glass which is designed to have high transparency in the visible regime. This leads to an experimental bias where even strong UV light produced will not be measured and therefore not considered in its impact on the surrounding biological environment. To correctly analyse UV peaks without significant bias, the transparency of fibres, lenses, objectives, and filters should be assessed, as well as the ability of the spectrometer to detect the UV range.

Lenses and filters created using borosilicate, N-BK7 or sapphire glass have substantial absorption and will easily completely block the detection of UV light. This includes microscope slides or coverslips if they are placed in the light collection path. Often the specialised coating layer on interference filters will also have significant UV absorption that prevents meaningful measurements. If optical components are required for filtering or analysis, a common choice of

material is calcium fluoride, due to its high UV/visible/NIR transmission as well as its robustness and affordability compared to other fluoride glasses. Fused silica or quartz glass components are also popular but do exert some small deviations to the true UV intensity due to slightly increased absorption over the UV-B range. This is small enough to be compensated for if a response curve is known, such as is done for optical components in commercial spectrofluorometer systems.

Most visible/NIR detectors based on silicon imaging sensors do have some sensitivity below 350 nm, but this generally decreases to approximately a quarter of the visible light quantum efficiency by 300 nm.[42,43] Many fixed grating systems ignore this range however in favour of the optimised resolution and efficiency across the visible and NIR range through the choice of grating material and position that is often detrimental to UV detection.

To examine the ability of a given spectrometer and collection optics to detect UV emission, mercury calibration lamps are useful sources of bright, sharp peaks in the UV and visible region with well-defined emission wavelengths.[44,45] These can be found as small, low-powered and portable sources for easy calibration of bench-top spectrometer systems. Strong lines are present across the UV-A, UV-B and UV-C range and detection of these lines is positive confirmation that a spectrometer system is appropriately capable of UV light detection.

Water and most buffer systems offer acceptable UV transmission to allow for fluorescence peak detection; however, biological media often do not. This includes intracellular analysis, where the high transmission of an infrared excitation source and the emitted visible light are not matched by any UV emission, which is effectively absorbed by many parts of the cell including proteins[46] and DNA.[47] The consequence of this is that measurements to detect UV emission from doped nanoparticles cannot be undertaken while in a biological medium. The lack of detected UV emission could be falsely interpreted as a lack of UV light being produced, when the

emission is simply much more strongly absorbed relative to the visible light or NIR emission, and potentially influencing the environment in ways that are unaccounted for.

## Potential impact of UV emission from UCNPs on the biological environment.

Most studies on the biological impact of UV radiation have been focused on skin cancer caused by UV light from the sun.[48,49] UV-C has the highest energy level and causes the greatest biological damage, followed by UV-B and then UV-A.[50] Biological damage from exposure to UV light is mainly caused by the absorption of UV light by intracellular biomacromolecules or photosensitizing interactions via exogenous or endogenous reactions that generate ROS.[51,52] The main mechanism of cell damage by UV-A radiation is the interaction of UV-A with cellular chromophores (which act as photosensitisers) to generate ROS that damage DNA and the proteins that repair damaged DNA.[53] UV-A absorption by cellular chromophores generates a pair of radicals, including a photosensitizer anion and a target cation. The photosensitiser anion can generate superoxide, which can be converted into hydrogen peroxide and hydroxyl group via a series of reactions. Guanine (one of the building blocks of DNA and RNA), when excited by UV-A, reacts with water to form 8-hydroxy-7,8-dihydroguanyl radical which then oxidises to 8-oxo-7,8-dihydroguanine (8-oxoGua) by reaction with molecular oxygen.[54] UV-B directly damages cellular DNA by forming bulky adducts such as double-stranded breaks (DSBs) and cyclobutane pyrimidine dimers (CPDs), as well as generating ROS like UV-A.[55] The UV-B radiation specifcally generates ROS following absorption by chromophores such as carotenoids, vitamin A, pyridoxamine, eumelanin and phaeomelanin, and heme groups.[56]

The wavelength and intensity of the light emitted, the exposure duration and biological sample type are important factors influencing the potential for cell damage in microscopy analysis.[57] The photosensitivity of U2OS, COS-7 and HeLa cells has been studied at 405, 488, 514 and 558 nm

irradiation wavelengths for SRM,[58] and the study used both pulsed and CW lasers. While 100% of cells survived exposure to 514 nm wavelength light, the higher energy 405 nm wavelength light led to all cells being unviable. This was despite the 514 nm wavelength experiments being performed at an exposure duration of 4 times longer and with a laser power 10 times higher than used in the 405 nm wavelength case. While this is concerning for cell viability in SRM applications, it is worth noting that the UV emissions from the UCNPs shown in our study are related to the emission of light by UCNPs after near IR excitation. The UCNP UV emissions have lower fluxes in comparison to excitation laser used in the above study.

The as-synthesised UCNP samples emit three peaks in the UV region at 361 nm ($^1D_2 \rightarrow {}^3H_6$), 345 nm ($^1I_6 \rightarrow {}^3F_4$) and 290 nm ($^1I_6 \rightarrow {}^3H_6$), with the Gd doped UCNPs samples showing an additional peak at 311 nm ($^6P_{7/2} \rightarrow {}^8S_{7/2}$)[59]. The amount of UV- A and B generated by UCNP probes may not cause an immediate impact on the biological samples being examined by SRM; however, these UV emissions could cause phototoxicity in long dynamic imaging of live cells or more sensitive biological samples using SRM. Therefore, a consideration particularly needs to be given to the effects over a longer experiment or if the high excitation laser power is used in combination with particular UCNP fluorophores. In terms of the improvement of existing UCNP fluorophores or the development of new materials, there are opportunities to reduce the UV-A and B generation by modifying dopant types and ratios used.

# CONCLUSIONS

UCNPs are in continuous development as fluorescence probes for the SRM due to their inherently favourable photoluminescence characteristics. This study evaluated the UV emissions generated from UCNPs that have the potential to cause phototoxicity (cell damage). Eight

combinations of Yb/Tm and Yb/Tm/Gd doped UCNPs were synthesised and the UCNPs were excited by pulsed or continuous wave (CW) lasers.

We found that a lower Tm activator loading, of 1 mol%, in a $NaYF_4$:Yb/Tm UCNP will lead to higher UV-A and B emissions relative to the desired emission at 475 nm when excited by a pulsed or CW laser. However, in UCNPs with a $NaYbF_4$:Tm structure, NPs with an intermediate Tm loading of 2.5 and 5 mol% showed higher UV emissions compared to 1 and 10 mol% doped materials when excited by both pulsed and CW lasers. Moreover, for $NaYF_4$:Yb/Tm/Gd nanoparticles, samples excited by the CW laser showed significantly higher UV emissions compared with a pulsed laser excitation methodology. Importantly, the work has shown that most samples emitted UV radiation but that the dopant concentration and the ratio of activator to sensitiser have a significant impact on the amount of UV generated relative to the desired visible emission at 475 nm. The use of pulsed or CW lasers for excitation of the UCNPs also leads to a large variation in the amount of UV light produced relative to the visible emission.

Overall, these combined results highlight the importance of carefully tailoring the upconversion dopant concentration, as well as undertaking detailed fluorescent analysis on synthesised UCNPs. These detailed spectroscopic studies need to consider the challenges of measuring emitted UV light and the experimental biases present in standard characterisation workflows and apparatus. These actions are deemed necessary to prevent potential unwanted cell photodamage during live cell imaging by SRM and to improve the performance of new UCNPs being developed for SRM applications.

# EXPERIMENTAL SECTION

**Raw materials.** Gadolinium (III) chloride hexahydrate (Sigma-Aldrich, 99%), thulium (III) chloride (Sigma-Aldrich, 99.9%), ytterbium(III) chloride hexahydrate (Sigma–Aldrich, 99.9%),

yttrium (III) chloride hexahydrate (Sigma-Aldrich, 99.9%), ammonium fluoride (Chem–Supply, 98%), sodium hydroxide (Sigma–Aldrich, 99.99%), 1-octadecene (Sigma–Aldrich, technical grade, 90%), Oleic acid (Sigma-Aldrich, technical grade, 90%), methanol (Sigma–Aldrich, 99.9%), ethanol (Chem–Supply, 100%) and cyclohexane (Chem–Supply) were obtained from commercial sources and used without further purification.

**Synthesis of nanoparticles.** The NaYb(100-x)F4:Tm(x) (x = 1, 2.5, 5 and 10 mol%) and NaYb(100-x)$F_4$:Tm(0.5%)/Gd(x) (x = 5 and 20 mol%) were synthesized via a similar method to that previously reported[18] with slight modifications. NaYb(100-x)$F_4$:Tm(x) (x = 1, 2.5, 5 and 10 mol%) and NaYb(100-x)$F_4$:Tm(0.5%)/Gd(x) (x = 5 and 20 mol%) were synthesized via the same method with the following modifications: after the addition of the NaOH/$NH_4F$ solution and evaporation of methanol, the suspension was heated to 160 °C for 1h then to 320 °C for 40 minutes.[24]

**Characterization.** Powder X-ray diffraction (PXRD) data were collected on a MiniFlex 600 (Rigaku, Cu Kα, λ = 0.15418 nm). Samples were mounted in a flat plate holder and the data was collected with the instrument operating at 40 kV and 15 mA by scanning 2θ from 10° to 70° with a step size of 0.02°. The hexagonal structure β-$NaYbF_4$ (JCPDS # 27-1427), cubic structure α-$NaYbF_4$ (JCPDS # 77-2043), hexagonal structure β-$NaYF_4$ (JCPDS # 16-0334) and cubic structure α-$NaYF_4$ (JCPDS # 06-0342) were used for comparison to the experimental data.

Scanning electron microscopy (SEM) was conducted on a Quanta 450, and transmission electron microscopy (TEM) on an FEI Tecnai G2 Spirit TEM operated at an accelerating voltage of 120 kV. The NP samples were coated with platinum (3 nm) before SEM measurements. Samples for TEM were dispersed in absolute ethanol using a vortex shaker, a small droplet of

each suspension was transferred to the TEM sample holder, and the ethanol evaporated before placing into the TEM.

ICP−MS was conducted on an Agilent 8900x ICP-MS/MS instrument. A series of mixed element standard solutions were used to determine the calibration curve needed to quantify Y, Yb, Gd and Tm. Calibration standard solutions with concentrations of 10, 50, 100, 200 and 500 ppb were prepared using HPS-Q17617A (High Purity Standard, 10 mg/L in 2% $HNO_3$) solution. The NP samples were digested in $HNO_3$ (70% v/v) and then diluted in $HNO_3$ (2% v/v) to concentrations of 100 ppb for each NP sample. Pure $HNO_3$ (2% v/v) was also used as the control (blank sample). The plasma conditions of RF power 1,550 W, sample depth 10 mm and Ar carrier gas flow rate of 0.95 L/min and makeup gas flow rate of 0.1 L/min with a Micro Mist nebuliser and Scott Type spray chamber were used for measurements. The collision cell was run in He mode (4 ml/min He gas flow) for the following isotopes: 89Y, 173Yb, 157Gd, and 169Tm. Online addition of Indium was used as the internal standard element.

Photoluminescence measurements were carried out under 980 nm excitation using both a CW and pulsed laser. A fixed amount of powdered NP sample was used in the experiment for each sample. In the case of the pulsed laser, the samples were excited by pulses with a 5 ns duration and 20 Hz repetition rate from an Optical Parametric Oscillator (OPO) (Opotek LLC model "Opolette 355"). An 840 nm long-pass filter was placed before the sample to block visible wavelengths present in the OPO beam, and a silica lens was used to focus the spot size of the laser to approximately 2 mm. For the CW laser case, the samples were excited by MDL-III-980 diode laser at 980 nm. The emission spectra were collected using a spectrofluorometer (Edinburgh Instruments F980) with an air-cooled photomultiplier (Hamamatsu R928) for detection (Figure S12). The emission spectra were collected across the 280 to 630 nm detection

range of the photomultiplier. CW laser power dependence scans were conducted using the 980 nm laser diode through a continuous neutral density filter with a SpectraPro SP-2300i spectrometer and PIXIS 100 CCD sensor for detection. Pulsed laser energy dependence data were conducted using a Radiant X30 OPO set at 980 nm (5 ns pulses at a repetition rate of 10 Hz), with variations in energy enabled by rotation of two Glan-laser calcite polarisers placed in the beam path. UV emission was collected through a 340 nm short pass absorptive filter while visible light was collected through a 770 nm short pass interference filter.

# ASSOCIATED CONTENT

## Supporting Information

Supporting Information Available: PXRD data, ICP-MS data, EDS elemental analysis, and the TEM analysis with particle size measurements. This material is available free of charge via the Internet at http://pubs.acs.org

## Funding Sources

Cooperative Research Centre for Optimising Resource Extraction (Project P1-005); Commonwealth Government Department of Defence, Next Generation Technologies Fund, Grand Challenge-Counter Improvised Threats (CIED, Grant CIT-186); Australian Government Research Training Program Scholarship; The University of Adelaide.

# ACKNOWLEDGEMENTS

The support from the Australian Government Research Training Program Scholarship, Alice Chu postgraduate scholarship in Chemical Engineering, and The University of Adelaide is acknowledged. The upconversion facility was enabled by a LIEF grant (code LE140100042), and funding by CRC – Optimising Resource Extraction (ORE) project P1-005, and

Commonwealth Government Department of Defence, Next Generation Technologies Fund, Grand Challenge-Counter Improvised Threats (CIED) grant CIT-186 is acknowledged.

The authors acknowledge the instruments and scientific and technical assistance of Microscopy Australia at Adelaide Microscopy, The University of Adelaide, a facility that is funded by the university and state and federal governments. The table of contents (ToC) image was created with BioRender.com.

# REFERENCES

(1) Zhang, H.; Zhao, M.; Ábrahám, I. M.; Zhang, F. Super-Resolution Imaging With Lanthanide Luminescent Nanocrystals: Progress and Prospect. *Front Bioeng Biotechnol* **2021**, *9*, 692075. DOI: 10.3389/fbioe.2021.692075.
(2) Dong, H.; Sun, L.-D.; Yan, C.-H. Lanthanide-Doped Upconversion Nanoparticles for Super-Resolution Microscopy. *Frontiers in Chemistry* **2021**, *8*. DOI: 10.3389/fchem.2020.619377.
(3) Valli, J.; Garcia-Burgos, A.; Rooney, L. M.; Vale de Melo e Oliveira, B.; Duncan, R. R.; Rickman, C. Seeing beyond the limit: A guide to choosing the right super-resolution microscopy technique. *J. Biol. Chem.* **2021**, *297* (1), 100791. DOI: 10.1016/j.jbc.2021.100791.
(4) Jing, Y.; Zhang, C.; Yu, B.; Lin, D.; Qu, J. Super-Resolution Microscopy: Shedding New Light on In Vivo Imaging. *Frontiers in chemistry* **2021**, *9*, 746900-746900. DOI: 10.3389/fchem.2021.746900.
(5) Sigal, Y. M.; Zhou, R.; Zhuang, X. Visualizing and discovering cellular structures with super-resolution microscopy. *Science* **2018**, *361* (6405), 880-887. DOI: 10.1126/science.aau1044.
(6) Yang, Z.; Samanta, S.; Yan, W.; Yu, B.; Qu, J. Super-resolution Microscopy for Biological Imaging. In *Adv Exp Med Biol*, Vol. 3233; 2021; pp 23-43.
(7) De Camillis, S.; Ren, P.; Cao, Y.; Plöschner, M.; Denkova, D.; Zheng, X.; Lu, Y.; Piper, J. A. Controlling the non-linear emission of upconversion nanoparticles to enhance super-resolution imaging performance. *Nanoscale* **2020**, *12* (39), 20347-20355. DOI: 10.1039/D0NR04809G.
(8) Yadav, A.; Rao, C.; Nandi, C. K. Fluorescent Probes for Super-Resolution Microscopy of Lysosomes. *ACS Omega* **2020**, *5* (42), 26967-26977. DOI: 10.1021/acsomega.0c04018.
(9) Li, W.; Kaminski Schierle, G. S.; Lei, B.; Liu, Y.; Kaminski, C. F. Fluorescent Nanoparticles for Super-Resolution Imaging. *Chem. Rev.* **2022**, *122* (15), 12495-12543. DOI: 10.1021/acs.chemrev.2c00050.
(10) Cheng, L.; Wang, C.; Liu, Z. Upconversion nanoparticles and their composite nanostructures for biomedical imaging and cancer therapy. *Nanoscale* **2013**, *5* (1), 23-37. DOI: 10.1039/C2NR32311G.
(11) Chen, C.; Wang, F.; Wen, S.; Su, Q. P.; Wu, M. C. L.; Liu, Y.; Wang, B.; Li, D.; Shan, X.; Kianinia, M.; Aharonovich, I.; Toth, M.; Jackson, S. P.; Xi, P.; Jin, D. Multi-photon near-infrared emission saturation nanoscopy using upconversion nanoparticles. *Nature Communications* **2018**, *9* (1), 3290. DOI: 10.1038/s41467-018-05842-w.
(12) Zhan, Q.; Liu, H.; Wang, B.; Wu, Q.; Pu, R.; Zhou, C.; Huang, B.; Peng, X.; Ågren, H.; He, S. Achieving high-efficiency emission depletion nanoscopy by employing cross relaxation in upconversion nanoparticles. *Nature Communications* **2017**, *8* (1), 1058. DOI: 10.1038/s41467-017-01141-y.
(13) Wen, S.; Zhou, J.; Zheng, K.; Bednarkiewicz, A.; Liu, X.; Jin, D. Advances in highly doped upconversion nanoparticles. *Nature Communications* **2018**, *9* (1), Review article. DOI: 10.1038/s41467-018-04813-5.

(14) Maurizio, S. L.; Tessitore, G.; Mandl, G. A.; Capobianco, J. A. Luminescence dynamics and enhancement of the UV and visible emissions of $Tm^{3+}$ in $LiYF_4:Yb^{3+},Tm^{3+}$ upconverting nanoparticles. *Nanoscale Advances* **2019**, *1* (11), 4492-4500. DOI: 10.1039/C9NA00556K.
(15) Zheng, B.; Fan, J.; Chen, B.; Qin, X.; Wang, J.; Wang, F.; Deng, R.; Liu, X. Rare-Earth Doping in Nanostructured Inorganic Materials. *Chem. Rev.* **2022**, *122* (6), 5519-5603. DOI: 10.1021/acs.chemrev.1c00644.
(16) Wei, H.-L.; Zheng, W.; Zhang, X.; Suo, H.; Chen, B.; Wang, Y.; Wang, F. Tuning Near-Infrared-to-Ultraviolet Upconversion in Lanthanide-Doped Nanoparticles for Biomedical Applications. *Advanced Optical Materials* **2022**, *n/a* (n/a), 2201716. DOI: 10.1002/adom.202201716.
(17) Yu, T. h.; Xuan, Y.; Wang, X.; Yan, X. Infrared excitation induced upconversion fluorescence properties and photoelectric effect of $NaYbF_4:Tm^{3+}@TiO_2$ core–shell nanoparticles. *RSC Advances* **2014**, *4* (90), 49415-49420. DOI: 10.1039/C4RA06488G.
(18) Karami, A.; Farivar, F.; de Prinse, T. J.; Rabiee, H.; Kidd, S.; Sumby, C. J.; Bi, J. Facile Multistep Synthesis of ZnO-Coated β-NaYF4:Yb/Tm Upconversion Nanoparticles as an Antimicrobial Photodynamic Therapy for Persistent Staphylococcus aureus Small Colony Variants. *ACS Applied Bio Materials* **2021**, *4* (8), 6125-6136. DOI: 10.1021/acsabm.1c00473.
(19) Wei, J.; Zhao, H.; Zhang, L.; Chai, S.; Liu, H.; Wang, Y.; Xue, J. Vis-UV Upconverting bacteriostatic hydrophobic bacterial cellulose film for personal protective masks. *Carbohydr. Polym.* **2022**, *297*, 119967. DOI: 10.1016/j.carbpol.2022.119967.
(20) Shen, J.; Chen, G.; Ohulchanskyy, T. Y.; Kesseli, S. J.; Buchholz, S.; Li, Z.; Prasad, P. N.; Han, G. Tunable Near Infrared to Ultraviolet Upconversion Luminescence Enhancement in (α-$NaYF_4$:Yb,Tm)/$CaF_2$ Core/Shell Nanoparticles for In situ Real-time Recorded Biocompatible Photoactivation. *Small* **2013**, *9* (19), 3213-3217. DOI: 10.1002/smll.201300234.
(21) Sharma, V. K.; Demir, H. V. Bright Future of Deep-Ultraviolet Photonics: Emerging UVC Chip-Scale Light-Source Technology Platforms, Benchmarking, Challenges, and Outlook for UV Disinfection. *ACS Photonics* **2022**, *9* (5), 1513-1521. DOI: 10.1021/acsphotonics.2c00041.
(22) Tosheva, K. L.; Yuan, Y.; Matos Pereira, P.; Culley, S.; Henriques, R. Between life and death: strategies to reduce phototoxicity in super-resolution microscopy. *J. Phys. D: Appl. Phys.* **2020**, *53* (16), 163001. DOI: 10.1088/1361-6463/ab6b95.
(23) de Prinse, T. J.; Karami, A.; Moffatt, J. E.; Payten, T. B.; Tsiminis, G.; Teixeira, L. D. S.; Bi, J.; Kee, T. W.; Klantsataya, E.; Sumby, C. J.; Spooner, N. A. Dual Laser Study of Non-Degenerate Two Wavelength Upconversion Demonstrated in Sensitizer-Free $NaYF_4$:Pr Nanoparticles. *Advanced Optical Materials* **2021**, *9* (7), 2001903. DOI: 10.1002/adom.202001903.
(24) Shi, R.; Ling, X.; Li, X.; Zhang, L.; Lu, M.; Xie, X.; Huang, L.; Huang, W. Tuning hexagonal $NaYbF_4$ nanocrystals down to sub-10 nm for enhanced photon upconversion. *Nanoscale* **2017**, *9* (36), 13739-13746. DOI: 10.1039/C7NR04877G.
(25) Xu, R.; Cao, H.; Lin, D.; Yu, B.; Qu, J. Lanthanide-doped upconversion nanoparticles for biological super-resolution fluorescence imaging. *Cell Reports Physical Science* **2022**, *3* (6), 100922. DOI: 10.1016/j.xcrp.2022.100922.
(26) Huang, B.; Wu, Q.; Peng, X.; Yao, L.; Peng, D.; Zhan, Q. One-scan fluorescence emission difference nanoscopy developed with excitation orthogonalized upconversion nanoparticles. *Nanoscale* **2018**, *10* (45), 21025-21030, 10.1039/C8NR07017B. DOI: 10.1039/C8NR07017B.
(27) Zhao, J.; Jin, D.; Schartner, E. P.; Lu, Y.; Liu, Y.; Zvyagin, A. V.; Zhang, L.; Dawes, J. M.; Xi, P.; Piper, J. A.; Goldys, E. M.; Monro, T. M. Single-nanocrystal sensitivity achieved by enhanced upconversion luminescence. *Nature Nanotechnology* **2013**, *8* (10), 729-734. DOI: 10.1038/nnano.2013.171.
(28) Algar, W. R.; Massey, M.; Rees, K.; Higgins, R.; Krause, K. D.; Darwish, G. H.; Peveler, W. J.; Xiao, Z.; Tsai, H.-Y.; Gupta, R.; Lix, K.; Tran, M. V.; Kim, H. Photoluminescent Nanoparticles for Chemical and Biological Analysis and Imaging. *Chem. Rev.* **2021**, *121* (15), 9243-9358. DOI: 10.1021/acs.chemrev.0c01176.

(29) Chen, G. Y.; Qiu, H. Q.; Prasad, P. N.; Chen, X. Y. Upconversion Nanoparticles: Design, Nanochemistry, and Applications in Theranostics. *Chem. Rev.* **2014**, *114*, 5161.
(30) Pu, R.; Zhan, Q.; Peng, X.; Liu, S.; Guo, X.; Liang, L.; Qin, X.; Zhao, Z. W.; Liu, X. Super-resolution microscopy enabled by high-efficiency surface-migration emission depletion. *Nature Communications* **2022**, *13* (1), 6636. DOI: 10.1038/s41467-022-33726-7.
(31) Damasco, J. A.; Chen, G.; Shao, W.; Ågren, H.; Huang, H.; Song, W.; Lovell, J. F.; Prasad, P. N. Size-Tunable and Monodisperse $Tm^{3+}/Gd^{3+}$-Doped Hexagonal $NaYbF_4$ Nanoparticles with Engineered Efficient Near Infrared-to-Near Infrared Upconversion for In Vivo Imaging. *ACS Applied Materials & Interfaces* **2014**, *6* (16), 13884-13893. DOI: 10.1021/am503288d.
(32) Dong, H.; Sun, L.-D.; Yan, C.-H. Energy transfer in lanthanide upconversion studies for extended optical applications. *Chem. Soc. Rev.* **2015**, *44* (6), 1608-1634, Review article. DOI: 10.1039/C4CS00188E.
(33) Wang, F.; Liu, X. G. Multicolor Tuning of Lanthanide-Doped Nanoparticles by Single Wavelength Excitation. *Acc. Chem. Res.* **2014**, *47*, 1378.
(34) Wang, L.; Li, X.; Li, Z.; Chu, W.; Li, R.; Lin, K.; Qian, H.; Wang, Y.; Wu, C.; Li, J.; Tu, D.; Zhang, Q.; Song, L.; Jiang, J.; Chen, X.; Luo, Y.; Xie, Y.; Xiong, Y. A new cubic phase for a $NaYF_4$ host matrix offering high upconversion luminescence efficiency. *Adv. Mater.* **2015**, *27* (37), 5528-5533. DOI: 10.1002/adma.201502748.
(35) Vidyakina, A. A.; Kolesnikov, I. E.; Bogachev, N. A.; Skripkin, M. Y.; Tumkin, I. I.; Lähderanta, E.; Mereshchenko, A. S. $Gd^{3+}$-Doping Effect on Upconversion Emission of $NaYF_4$: $Yb^{3+}$, $Er^{3+}/Tm^{3+}$ Microparticles. *Materials (Basel, Switzerland)* **2020**, *13* (15), 3397. DOI: 10.3390/ma13153397.
(36) Moffatt, J. E.; Tsiminis, G.; Klantsataya, E.; de Prinse, T. J.; Ottaway, D.; Spooner, N. A. A practical review of shorter than excitation wavelength light emission processes. *Applied Spectroscopy Reviews* **2020**, *55* (4), 327-349. DOI: 10.1080/05704928.2019.1672712.
(37) Pollnau, M.; Gamelin, D. R.; Lüthi, S. R.; Güdel, H. U.; Hehlen, M. P. Power dependence of upconversion luminescence in lanthanide and transition-metal-ion systems. *Physical Review B* **2000**, *61* (5), 3337-3346. DOI: 10.1103/PhysRevB.61.3337.
(38) Vidyakina, A. A.; Kolesnikov, I. E.; Bogachev, N. A.; Skripkin, M. Y.; Tumkin, I. I.; Lähderanta, E.; Mereshchenko, A. S. $Gd^{3+}$-Doping Effect on Upconversion Emission of NaYF4: $Yb^{3+}$, $Er^{3+}/Tm^{3+}$ Microparticles. *Materials* **2020**, *13* (15), 3397. DOI: 10.3390/ma13153397.
(39) Quintanilla, M.; Cantarelli, I. X.; Pedroni, M.; Speghini, A.; Vetrone, F. Intense ultraviolet upconversion in water dispersible SrF2:Tm3+,Yb3+ nanoparticles: the effect of the environment on light emissions. *Journal of Materials Chemistry C* **2015**, *3* (13), 3108-3113, 10.1039/C4TC02791D. DOI: 10.1039/C4TC02791D.
(40) Shang, Y.; Zhou, J.; Cai, Y.; Wang, F.; Fernandez-Bravo, A.; Yang, C.; Jiang, L.; Jin, D. Low threshold lasing emissions from a single upconversion nanocrystal. *Nature Communications* **2020**, *11* (1), 6156. DOI: 10.1038/s41467-020-19797-4.
(41) Plöschner, M.; Denkova, D.; De Camillis, S.; Das, M.; Parker, L. M.; Zheng, X.; Lu, Y.; Ojosnegros, S.; Piper, J. A. Simultaneous super-linear excitation-emission and emission depletion allows imaging of upconversion nanoparticles with higher sub-diffraction resolution. *Opt. Express* **2020**, *28* (16), 24308-24326. DOI: 10.1364/OE.400651.
(42) Greer, F.; Hamden, E.; Jacquot, B. C.; Hoenk, M. E.; Jones, T. J.; Dickie, M. R.; Monacos, S. P.; Nikzad, S. Atomically precise surface engineering of silicon CCDs for enhanced UV quantum efficiency. *Journal of Vacuum Science & Technology A* **2013**, *31* (1), 01A103.
(43) Yibin, B.; Jagmohan, B.; James, W. B.; Mark, C. F.; Atul, J.; Stefan, L.; Anders, P.; George, W. Teledyne Imaging Sensors: silicon CMOS imaging technologies for x-ray, UV, visible, and near infrared. In *Proc.SPIE*, 2008; Vol. 7021, p 702102. DOI: 10.1117/12.792316.
(44) Zacharioudaki, D. E.; Fitilis, I.; Kotti, M. Review of Fluorescence Spectroscopy in Environmental Quality Applications. *Molecules* **2022**, *27* (15). DOI: 10.3390/molecules27154801 From NLM.
(45) Sansonetti, C. J.; Salit, M. L.; Reader, J. Wavelengths of spectral lines in mercury pencil lamps. *Appl. Opt.* **1996**, *35* (1), 74-77. DOI: 10.1364/AO.35.000074.

(46) Khoroshilova, E. V.; Repeyev, Y. A.; Nikogosyan, D. N. UV protolysis of aromatic amino acids and related dipeptides and tripeptides. *Journal of Photochemistry and Photobiology B: Biology* **1990**, *7* (2), 159-172. DOI: 10.1016/1011-1344(90)85153-N.
(47) Besaratinia, A.; Yoon, J. I.; Schroeder, C.; Bradforth, S. E.; Cockburn, M.; Pfeifer, G. P. Wavelength dependence of ultraviolet radiation-induced DNA damage as determined by laser irradiation suggests that cyclobutane pyrimidine dimers are the principal DNA lesions produced by terrestrial sunlight. *FASEB J.* **2011**, *25* (9), 3079-3091. DOI: 10.1096/fj.11-187336 From NLM.
(48) Tripp, M. K.; Watson, M.; Balk, S. J.; Swetter, S. M.; Gershenwald, J. E. State of the Science on Prevention and Screening to Reduce Melanoma Incidence and Mortality: The Time Is Now. *CA Cancer J. Clin.* **2016**, *66* (6), 460-480. DOI: 10.3322/caac.21352.
(49) Boo, Y. C. Emerging Strategies to Protect the Skin from Ultraviolet Rays Using Plant-Derived Materials. *Antioxidants* **2020**, *9* (7), 637.
(50) Lo, C.-W.; Matsuura, R.; Iimura, K.; Wada, S.; Shinjo, A.; Benno, Y.; Nakagawa, M.; Takei, M.; Aida, Y. UVC disinfects SARS-CoV-2 by induction of viral genome damage without apparent effects on viral morphology and proteins. *Sci. Rep.* **2021**, *11* (1), 13804. DOI: 10.1038/s41598-021-93231-7.
(51) Mullenders, L. H. F. Solar UV damage to cellular DNA: from mechanisms to biological effects. *Photochemical & Photobiological Sciences* **2018**, *17* (12), 1842-1852. DOI: 10.1039/c8pp00182k.
(52) Nawkar, G. M.; Maibam, P.; Park, J. H.; Sahi, V. P.; Lee, S. Y.; Kang, C. H. UV-Induced Cell Death in Plants. *Int. J. Mol. Sci.* **2013**, *14* (1), 1608-1628.
(53) Santos, A. L.; Oliveira, V.; Baptista, I.; Henriques, I.; Gomes, N. C. M.; Almeida, A.; Correia, A.; Cunha, Â. Wavelength dependence of biological damage induced by UV radiation on bacteria. *Arch. Microbiol.* **2013**, *195* (1), 63-74. DOI: 10.1007/s00203-012-0847-5.
(54) Brem, R.; Guven, M.; Karran, P. Oxidatively-generated damage to DNA and proteins mediated by photosensitized UVA. *Free Radical Biology and Medicine* **2017**, *107*, 101-109. DOI: 10.1016/j.freeradbiomed.2016.10.488.
(55) Kim, D. J.; Iwasaki, A.; Chien, A. L.; Kang, S. UVB-mediated DNA damage induces matrix metalloproteinases to promote photoaging in an AhR- and SP1-dependent manner. *JCI Insight* **2022**, *7* (9). DOI: 10.1172/jci.insight.156344.
(56) Pattison, D. I.; Davies, M. J. Actions of ultraviolet light on cellular structures. In *Cancer: Cell Structures, Carcinogens and Genomic Instability*, Birkhäuser Basel, 2006; pp 131-157.
(57) Laissue, P. P.; Alghamdi, R. A.; Tomancak, P.; Reynaud, E. G.; Shroff, H. Assessing phototoxicity in live fluorescence imaging. *Nature Methods* **2017**, *14* (7), 657-661. DOI: 10.1038/nmeth.4344.
(58) Wäldchen, S.; Lehmann, J.; Klein, T.; van de Linde, S.; Sauer, M. Light-induced cell damage in live-cell super-resolution microscopy. *Sci. Rep.* **2015**, *5* (1), 15348. DOI: 10.1038/srep15348.
(59) Chen, X.; Jin, L.; Kong, W.; Sun, T.; Zhang, W.; Liu, X.; Fan, J.; Yu, S. F.; Wang, F. Confining energy migration in upconversion nanoparticles towards deep ultraviolet lasing. *Nature Communications* **2016**, *7* (1), 10304. DOI: 10.1038/ncomms10304.